



# Confluence of channel dimensions and groove width dictates slippery hydrodynamics in grooved hydrophobic confinements

Prasenjit Dey<sup>1</sup> · Sandip K. Saha<sup>1</sup> · Suman Chakraborty<sup>2</sup>

Received: 11 July 2019 / Accepted: 22 October 2019 / Published online: 13 March 2020  
© Springer-Verlag GmbH Germany, part of Springer Nature 2020

## Abstract

Slippery hydrodynamics in grooved hydrophobic microchannels is known to be primarily dictated by the area of the gas–liquid contact surface. Here, we augment this classical notion by bringing out the critical role played by the channel dimensions on the underlying slip mechanisms and the consequent drag reduction. Our analysis, towards this, reveals the non-trivial implication of gas–liquid interface topology and its position inside the groove towards dictating the underlying frictional characteristics, which in turn is largely dependent on the confluence of the channel hydraulic diameter and the groove width. These results may turn out to be of immense consequence towards arriving at preferred frictional drag characteristics of hydrophobic microchannels and nanochannels by judicious choices of the pertinent geometric parameters.

**Keywords** Superhydrophobic · Scale effect · Slip characteristic · Interface shape

## 1 Introduction

Superhydrophobic surfaces (*SPHS*) have drawn great interest due to remarkable developments in their applications in microfluidic and nanofluidic arena, including the development of self-cleaning (Fürstner et al. 2005) and bio-fouling surfaces (Genzer and Efimenko 2006), biomimetics (Liu and Kim 2014; Nosonovsky and Bhushan 2009), frictional drag reduction (Jung and Bhushan 2009), filtration (Holt 2006), desalination (Zhao et al. 2013), energy conversion (Chakraborty et al. 2013), and biomolecule sequencing (Chen et al. 2018). Superhydrophobicity is a phenomenon that results from a combination of hydrophobicity and micro/nano roughness (Ou and Rothstein 2005). Numerous studies have been dedicated to quantify the reduction in the skin-friction drag on submerged objects or microchannels with superhydrophobic surfaces (Lauga and Stone 2003; Lee and Choi 2008; McHale et al. 2009; Ou and Rothstein 2005).

Several experimental and numerical studies have been conducted on microchannels with different

superhydrophobic surfaces with the primary goal to reduce the frictional drag. The design of superhydrophobic surfaces can be longitudinal or transverse (Cheng et al. 2015; Davies et al. 2006; Maynes et al. 2007; Ng and Wang 2009; Teo and Khoo 2014) depending on the flowing fluid direction. In a superhydrophobic microchannel, the pressure drop can be reduced up to 40% with an apparent slip length larger than 20  $\mu\text{m}$  using ultrahydrophobic micropost surfaces (Ou et al. 2004). However, hydrophobic surfaces without roughness are unable to produce significant drag in laminar flow condition. The drag reduction of flow over ultrahydrophobic micro-scale ridges can be attributed to the slip along the shear-free air–water interface between two adjacent ridges (Ou and Rothstein 2005), as the flowing liquid cannot penetrate that cavity regions, resulting in a significant reduction at the surface contact area between the flowing liquid and the solid wall (Woolford et al. 2005). Therefore, a considerable reduction in the frictional pressure drop can be achieved. A maximum effective slip length of 20  $\mu\text{m}$  was obtained using needle-like roughness with varying height and submicron periodicity (i.e., pitch) (Choi and Kim 2006). The effective slip length significantly depends on the interface curvature or the contact angle at the triple line/point (Chakraborty et al. 2012; Teo and Khoo 2010; Tsai et al. 2009). The heterogeneities of the confining walls in microfluidic channel influence the contact angle. Hence, the wetting condition of the wall surface has significant impact on the contact line

✉ Sandip K. Saha  
sandip.saha@iitb.ac.in

<sup>1</sup> Department of Mechanical Engineering, Indian Institute of Technology Bombay, Mumbai 400076, India

<sup>2</sup> Department of Mechanical Engineering, Indian Institute of Technology Kharagpur, Kharagpur 721302, India

movement (Chakraborty et al. 2012). Also, the surface characteristics have pronounced influence on the pressure-driven liquid transport through microchannels (Chakraborty 2007).

Further, experimental analyses of fluid flow in square, trapezoidal, and U-shaped SPHs microchannel were conducted. It was revealed that the slip behaviour depends on the geometric features of the confinement, which in turn is defined by the air–water interfacial topology and has impact on the Poiseuille number (Gaddam et al. 2015). A maximum of approximately 22% reduction on Poiseuille number, as compared to the plain channel scenario, was found at  $Re = 25$ . For a predefined air–water interface in different microgroove geometries, a slight reduction in the pressured drop was observed with increasing inlet velocity and a significant drag reduction could be achieved by increasing the cavity fraction (Li et al. 2016). A maximum of 15% pressure drop reduction was observed in parabolic type superhydrophobic surfaces. However, the amount of drag reduction decreased with Reynolds number and an order of 10% drag reduction was achieved on a hydrofoil with superhydrophobic coating (Gogte et al. 2005). Further, a drag reduction of 35% was found in a cylindrical microchannel fabricated by replicating lotus leaf structures on internal walls (Das and Bhaumik 2018). In a very recent study, solar photovoltaic/thermal (PV/T) systems were analyzed and an amount of 19% drag reduction was achieved for better solar collection with minimal fluid flow resistance (Motamedi et al. 2019).

In addition, the effect of wall confinement along with roughness pattern on the fluid slip was found significant. Pressure drop reductions as large as 35% were observed for a channel height,  $H = 76.2 \mu\text{m}$  with an ultrahydrophobic surface having a regular array of  $d = 30 \mu\text{m}$  square microposts. The pressure drop reduction was found to decrease linearly with increasing channel height (Ou et al. 2004). Similarly, it was observed that for longitudinal grooves, the channel wall confinement has positive influence on the effective slip properties; whereas, the transverse grooves have negative impact (Cheng et al. 2009). It was found that the pressure drop reduction rate decreased with increasing microchannel height, and an amount of 10.35% reduction on pressure drop was attained in a microchannel of hydraulic diameter of  $160 \mu\text{m}$  (Li et al. 2016). An experimental and numerical analysis suggested that no-slip boundary condition is more efficient to predict the frictional characteristics of the air–water interface than a shear-free one, which is widely assumed (Kim and Hidrovo 2012). Furthermore, it was noted by the authors that a substantial friction reduction (in the order of 15–18%) can be achieved in a rectangular microchannel with regular microtexturing on the sidewalls under fully wetted conditions. However, the hydrophobic microposts/ridges are distributed randomly in reality and also resembles the natural superhydrophobic surfaces (Samaha et al. 2011). A maximum of 30% drag reduction can be obtained

at a gas fraction of 0.98; however, the gas fraction strongly influences the meniscus stability. Thus, a very careful investigation is needed before fabricating such superhydrophobic surfaces.

While the area of the gas–liquid contact surface has been proved to be one of the explicit influencing factors towards achieving drag reduction over superhydrophobic grooves, the implicit role played by the confining channel dimensions has not been critically investigated. Here, the same is addressed for incompressible flow in the continuum flow regime [Knudsen number ( $Kn < 0.01$ )], for which the effect of confluence of the width of superhydrophobic grooves and the confinement dimensions on the dynamic behavior of air–liquid interface, slip characteristics, and corresponding drag reduction are highlighted. A two-dimensional numerical model is developed by considering incompressible, Newtonian, laminar two-phase fluid flow to study the effect of the pertinent characteristic dimensions. Our results may turn out to be of immense consequence towards arriving at preferred channel dimensions for obtaining desired slip characteristics over miniaturized superhydrophobic grooves.

## 2 Definition of the physical problem

Figure 1 depicts the schematic illustration of the two-dimensional computational domain along with the boundary conditions. A plain microchannel of depth,  $D$  and length,  $L$  is used in the present numerical analysis. The hydraulic diameter,  $D_h = 2D$  is varied as,  $D_h = 600 \mu\text{m}$ ,  $60 \mu\text{m}$ ,  $6 \mu\text{m}$ , and  $600 \text{nm}$  to study the effect of transformation of microchannel to nanochannel on interface behavior, slip characteristics, and corresponding drag reduction. The least dimension is so chosen so as to confirm the justification of continuum formulation as adopted in the present study. At the bottom and top surfaces of the plain microchannel, triangular groove is introduced along the length of the channel. The geometry of the triangular microgroove is defined by its width ( $w$ ) and height ( $H$ ), where  $w$  is varied as,  $w/D_h = 0$  (plain channel),  $0.033$ ,  $0.067$  and  $0.133$  and  $H$  is taken constant as,  $H/D_h = 0$  (plain channel) and  $0.167$ . The velocity of incoming liquid or the free stream velocity,  $U_\infty$  is kept constant according to a fixed Reynolds number,  $Re = 1$ . The Reynolds number is defined based on the hydraulic diameter of the channel,  $D_h$  as,

$$Re = \frac{\rho_1 U_\infty D_h}{\mu_1}, \quad (1)$$

where,  $\rho_1$  and  $\mu_1$  are density and dynamic viscosity of the liquid phase. In the present study, the limits of Knudsen number ( $Kn$ ) and Mach number ( $Ma$ ) are kept as  $Kn < 0.01$  and  $Ma < 0.3$ , to treat the flow as incompressible in continuum

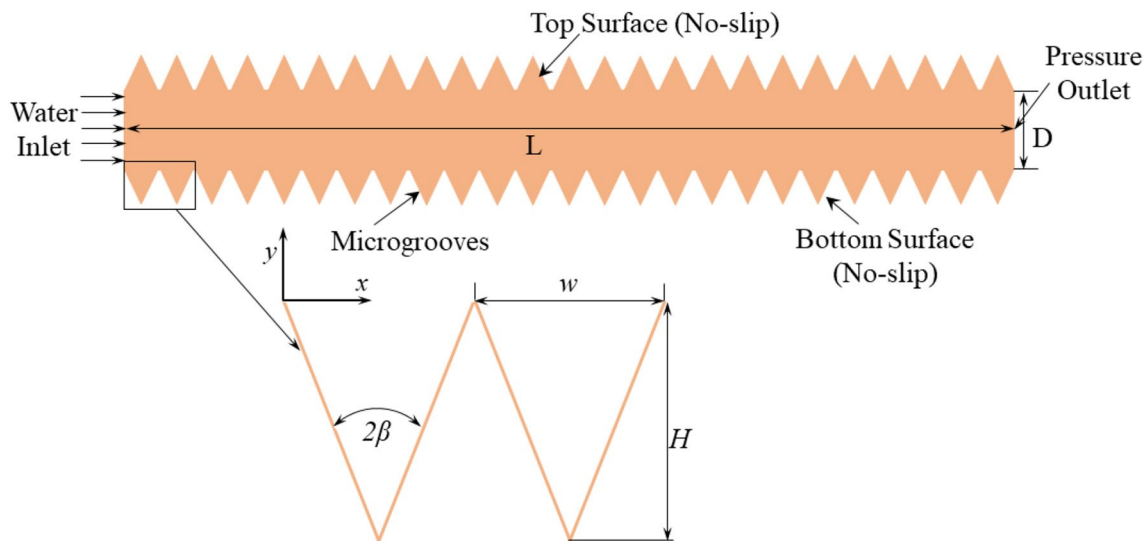


**Fig. 1** Schematic representation of the present numerical domain and the boundary conditions with an enlarged view of a triangular micro/nano groove

**Table 1** Thermophysical properties of water and air in simulations

Material	Density, $\rho$ (kg/m <sup>3</sup> )	Dynamic viscosity, $\mu$ (kg/m s)	Surface tension, $\sigma$ (N/m)
Water	998.2	$1.003 \times 10^{-3}$	0.0727
Air	1.225	$1.789 \times 10^{-5}$	–

flow regime; thus, the Reynolds number and the minimum value of hydraulic diameter in this study are limited to  $Re = 1$  and  $D_h \geq 600$  nm. The physical properties of water and air considered in the present analysis are given in Table 1.

It is assumed that the considered groove height is sufficient to hold up the liquid against the pressure of liquid ( $P_l$ ) over gas pressure ( $P_g$ ). Using geometrical calculation and the Laplace–Young equation, the post height  $H$  can be obtained as follows (Choi and Kim 2006),

$$H > \frac{1 - \sin(\theta - \beta)}{2|\cos(\theta - \beta)|} w. \tag{2}$$

At the initial stage ( $t^- = 0$ ), the computational domain is occupied by air and water is then ( $t^+ = 0$ ) allowed to flow through the channel from the inlet.

### 3 Mathematical formulation

The volume of fluid (VOF) method (Hirt and Nichols 1981) is used in this study to investigate the two-phase flow (air–water) behavior in the superhydrophobic microchannel patterned with transverse triangular microgrooves on the

top and bottom surfaces. The governing equations for mass, momentum and volume fraction are written assuming liquid and vapor as incompressible and Newtonian fluids. The VOF method models the flow by solving the momentum equation for the two fluids as if they were a homogeneous mixture; thus, density and velocity are volume-averaged. Hence, the volume-averaged continuity equation can be written as,

$$\nabla \cdot (\rho \vec{u}) = 0. \tag{3}$$

The volume of fluid in a cell is computed as,

$$F_{vol} = \phi V_{cell}, \tag{4}$$

where,  $V_{cell}$  is the volume of a computational cell. The range of  $\phi$  in a cell is 0–1.  $\phi = 1$ , if the cell is occupied by the fluid, whereas  $\phi = 0$  if the cell is filled with the void phase. At the interface, the value of  $\phi$  is between 0 and 1. The scalar function  $\phi$  can be determined from a separate transport equation, which is transported in a purely convective manner and is in the form of,

$$\frac{\partial \phi}{\partial t} + \nabla \cdot (\vec{u} \phi) = 0. \tag{5}$$

A counter-gradient transport scheme along with an algebraic approach is used in OpenFOAM (interFoam solver) to advect the volume fraction,  $\phi$  (Weller 1993). A compressive term is then incorporated by this technique in  $\alpha$  advection equation, (Eq. 5) to retain the conservativeness, convergence and boundedness (Weller 2008). Thus, the advection equation, (Eq. 4) is expressed as,

$$\frac{\partial \phi}{\partial t} + \nabla \cdot (\vec{u} \phi) + \nabla \cdot (\phi(1 - \phi) U_c) = 0, \tag{6}$$

where  $U_c$  is a compressive velocity field suitable to compress the interface. This artificial term is active only at the gas–liquid interface region due to the term  $\phi(1-\phi)$  and to avoid any dispersion, the compressive velocity acts in the direction normal to the interface. Thus, to satisfy the above condition, the compression velocity is multiplied by  $(\nabla\phi/|\nabla\phi|)$  and can be expressed as,

$$U_c = \min(c_\phi|\vec{u}|, \max(|\vec{u}|)) \frac{\nabla\phi}{|\nabla\phi|}, \tag{7}$$

where,  $c_\phi$  is a constant known as compression factor, which is used to improve the compression.

The volume fraction advection equation is solved using an additional limiter to cut-off the face fluxes at the critical values. The volume fraction convective term is calculated using the Van Leer second order total variation diminishing scheme (TVD) (Van Leer 1979), while the compressive term is discretized using the interface compression scheme described by (Weller 2008).

An infinitesimally small interface between two phases exists according to the theory; however, a region with sub-microscopic width in space represents that interface in reality. Thus, the interface needs to be resolved sharply. To accomplish this, a very common practice of a fine mesh resolution is adopted, at least in the regions of free-surface motion. To ensure boundedness of the phase fraction, independent of the numerical discretization schemes, the VOF method that is implemented in the present analysis does not solve Eq. (6) implicitly, rather uses a multidimensional universal limiter with explicit solution (MULES) algorithm (Greenshields 2015; Rusche 2003).

It is important to note that the mass is globally conserved in spite of the local source terms. Total amount of mass that is removed on the liquid side of the interface reappears on the vapor side. Thus, the momentum balance equation can be written as,

$$\frac{\partial \vec{u}}{\partial t} + \rho(\nabla \cdot \vec{u})u = -\nabla p + \nabla \cdot (\mu \nabla u) + \vec{f}_S, \tag{8}$$

where  $\rho$  and  $\mu$  are the average density and absolute viscosity in a cell, respectively, and they depend on the density and viscosity of each fluid at the cell and are defined as,

$$\rho = \phi\rho_l + (1-\phi)\rho_g, \tag{9}$$

$$\mu = \phi\mu_l + (1-\phi)\mu_g. \tag{10}$$

The subscripts l and g, signify liquid and gas, respectively.

No additional source term is needed to account for the phase change in the momentum balance equation. The momentum source term,  $\vec{f}_S$  in Eq. (8) represents volumetric surface tension force. The surface tension is a force, acting only at the surface

that is required to maintain equilibrium in such instances. It acts to balance the radially inward inter-molecular attractive force with the radially outward pressure gradient force across the surface. In regions where two fluids are separated, but one of them is not in the form of spherical bubbles, the surface tension acts to minimize free energy by decreasing the area of the interface. It can be shown that the pressure drop across the surface depends on the surface tension coefficient,  $\sigma$  and the surface curvature as measured by two radii in orthogonal directions,  $R_1$  and  $R_2$ ;

$$P_l - P_g = \sigma \left( \frac{1}{R_1} + \frac{1}{R_2} \right), \tag{11}$$

where,  $P_l - P_g$  is the pressure difference across the interface. The volumetric surface tension force is calculated using the continuum surface force model (CSF) without the density averaging proposed by (Brackbill et al. 1992),

$$\vec{f}_S = P_l - P_g = \sigma kn, \tag{12}$$

where,  $n$  is a unit vector normal to the interface and  $k$  is the curvature of the interface. The calculation procedure of  $n$  and  $k$  is discussed in next.

### 3.1 Normal and curvature calculation

The accurate calculation of normal ( $n$ ) and curvature ( $k$ ) from updated value of  $\phi$  from Eq. (6) is of utmost importance to develop a precise interface curvature (Malik et al. 2007). In the present model, the height function (HF) technology (Cummins et al. 2005; Francois et al. 2006; Sussman 2003) is adopted for calculating interface normal and curvature from well-resolved volume fraction data. The HF technology is implemented only at the interface cells ( $0 < \phi < 1$ ), where each interface cell is further divided into number of sub-cells (stencils). In the present model, the interface cell is constructed by either  $7 \times 3$  or  $3 \times 7$  stencils as shown in Fig. 2 (Afkhani and Bussmann 2008; Malik et al. 2007). The number of stencils allocated along the direction normal to the interface and then fluid height ( $h$ ) is calculated by integrating the volume fraction of each stencils located along the normal to the interface and is expressed as (Malik et al. 2007),

$$h_m = \sum_{n=j-3}^{n=j+3} \phi_{i,n} \Delta_{cell}, \quad m = i - 1, \text{ and } i + 1, \tag{13}$$

where,  $\Delta_{cell}$  is the size of the interface cell at location  $(i, j)$ .

The final value of cell-centered normal,  $n_{cell}$  and curvature,  $k_{cell}$  are calculated using the value of height,  $h$  as,

$$n_{cell} = \left[ \begin{matrix} h_{i+1} - h_{i-1} \\ -2\Delta_{cell} \end{matrix} \right], \tag{14}$$

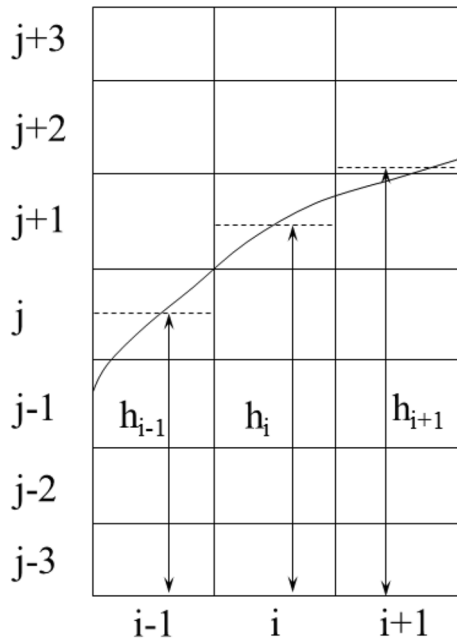


**Fig. 2** A 7 × 3 stencil used in the HF technology to calculate interface height

$$k_{\text{cell}} = \frac{h_{xx}}{(1 + h_x^2)^{3/2}}, \tag{15}$$

where,  $h_x$  and  $h_{xx}$  are the discretized functions and the second-order central difference scheme is used to discretize. Thus,  $h_x$  and  $h_{xx}$  are expressed as;

$$h_x = \frac{h_{i+1} - h_{i-1}}{2\Delta_{\text{cell}}}, \tag{16}$$

$$h_{xx} = \frac{h_{i+1} - 2h_i + h_{i-1}}{\Delta_{\text{cell}}^2}. \tag{17}$$

It is worth to mention here that the values of normal,  $n$  and curvature,  $k$  are calculated above are cell-centered; however, the face-centered values of  $n$  and  $k$  are required to calculate the surface tension force in Eq. (12). Thus, the cell-centered values are averaged to acquire the face-centered values.

### 3.2 Initial and boundary conditions

Initially, at  $t=0$ , the phase fraction in the numerical domain ( $x = 0$  to  $L$  and  $y = 0$  to  $(D + 2H)$ ) is  $\phi = 0$ .

The velocity boundary condition is applied at the inlet of the channel and is expressed as,

$$\text{At } x = 0, u(y) = U_{\infty}. \tag{18}$$

At the outlet, pressure condition is considered with pressure gradient zero,

$$\text{At } x = L, \nabla p = 0. \tag{19}$$

At the top and bottom surfaces, no-slip boundary condition is applied along with zero-gradient volume fraction,

$$u(x) \cdot \hat{n} = U_w \cdot \hat{n} = 0 \text{ and } \left. \frac{\partial \phi}{\partial n} \right|_{\text{wall}} = 0, \tag{20}$$

where,  $\hat{n}$  is the unit normal.

It needs to be noted that in the present study, the adhesion (contact angle) between the wall and interface (at the triple point) is not implemented using the static contact angle as the boundary condition. Rather, to model the wall adhesion between wall and interface (at the triple point), we adopt a zero-gradient ( $\left. \frac{\partial \phi}{\partial n} \right|_{\text{wall}} = 0$ ) type of boundary condition on volume fraction ( $\phi$ ). Since the contact angle description is not a pre-requisite of the implementation of the present method, an explicit advantage turns out to be obviating the needs of addressing contact angle hysteresis through prescribed sets of boundary conditions. Rather, the coupling of confinement, wettability and channel geometry implicitly takes care of this phenomenon via the adopted numerical procedure.

The present numerical analysis is executed in an open source CFD package, OpenFOAM (Greenshields 2015; Holzmann 2016). A multiphase solver interFoam is used to evaluate the two-phase flow behavior in the superhydrophobic microchannel. For the solution of two-phase equations of flow, the interFoam solver employs finite-volume discretization on the mixed collocated and staggered grids. The flow variables are cell centered; however, their face-interpolated values are also used in the solution procedure. In the present study, the HF technology is used to calculate normal,  $n$  and curvature,  $k$  that are further used to compute the value of surface tension force. The HF technology is developed in the existing multiphase solver, interFoam in OpenFOAM.

The PIMPLE scheme (Greenshields 2015; Holzmann 2016), which is a combination of PISO (Pressure Implicit with Splitting of Operator) and SIMPLE (Semi-Implicit Method for Pressure-Linked Equations) is used for pressure-velocity coupling. The time-derivative terms are discretized using a first-order implicit Euler scheme, controlling the time step by setting the maximum Courant number to 0.5. All the divergence and gradient terms are discretized using the second-order Gaussian linear integration scheme with van Leer limiter (Van Leer 1977). The solution is considered to be converged once the residuals reach  $10^{-6}$  for the continuity and  $10^{-9}$  for the pressure correction. The convergence criteria are chosen after conducting adequate convergence independence studies.

### 3.3 Validation of the present numerical model

The triangular microgroove is used as a superhydrophobic surface (roughness) in the present study at very low Reynolds number ( $Re = 1$ ) for investigating the effect of domain confinement on the air–water interface shape and position and the corresponding pressure drop numerically, by employing the volume of fluid (VOF) approach. The present numerical model is validated with the published experimental and numerical results of flow through a microchannel with square/rectangular microgrooves/microposts employed as a superhydrophobic surface. For the quantitative assessment, the normalized slip length of a microchannel with square micropost is considered (Cheng et al. 2009; Maynes et al. 2007). The normalized slip length can be calculated using the pressure drop,  $\Delta P$  and mass flow rate,  $\dot{m}$  within the microchannel and can be expressed as (Cheng et al. 2009),

$$\frac{l_s}{D/2} = \frac{8\mu\dot{m}}{\rho\Delta PD^3} - \frac{1}{3}. \tag{21}$$

The pressure drop can also be written in the non-dimensional form represented by Poiseuille number,  $fRe$ . In a steady, incompressible, laminar flow in a channel with smooth walls,  $fRe$  is expressed as (Cheng et al. 2009),

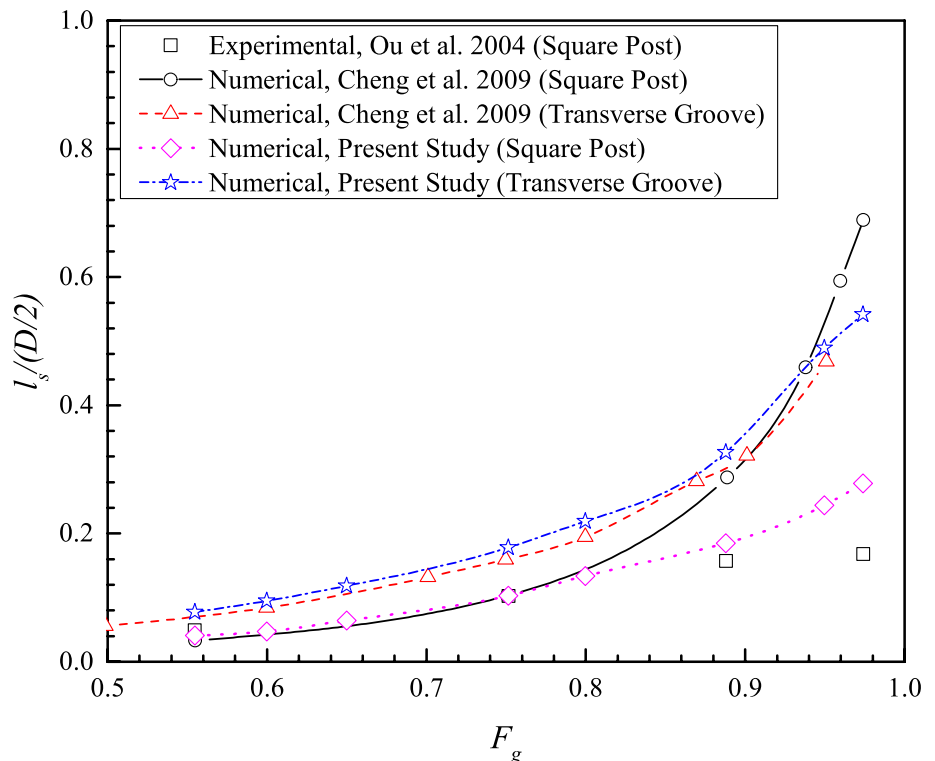
$$fRe = \frac{2\Delta p D_h^2}{U_\infty \mu_1 L}. \tag{22}$$

The normalized slip length is then calculated using Poiseuille number as,

$$\frac{l_s}{D/2} = \frac{32}{fRe} - \frac{1}{3} \tag{23}$$

The comparison between the present calculated normalized slip length and published experimental and numerical slip lengths for a regular array of  $30\ \mu\text{m}$  square microposts at  $Re = 1$  is depicted in Fig. 3. The gas fraction ( $F_g$ ) is varied as  $0.5 \leq F_g < 1$ . The gas fraction is defined as,  $F_g = w/w + d$ , where  $d$  is the gap between two successive microposts. It is observed that the present numerical model is in good agreement with the experimental data (Ou et al. 2004). It is also found that the slip length calculated by the present model is more accurate than that predicted by Cheng et al. (2009). The discrepancy in the prediction by Cheng et al. may be the result of predefined flat interface as well as the slip boundary assumption at the interface (Maynes et al. 2007; Cheng et al. 2009). When the interface is predefined as flat and the slip boundary condition is implemented at the interface in the transverse grooved microchannel, it can be seen that the present numerical model shows better agreement with the numerical data presented by Cheng et al. 2009 for all the considered values of  $F_g$ .

**Fig. 3** Validation of the present numerical study with reported numerical and experimental studies



## 4 Results and discussions

### 4.1 Effect of channel confinement on velocity distribution

The effect of channel confinement on the averaged (time and space) normalized velocity ( $u^* = u/U_{\max}$ ) distribution along the height of the channel for  $Re=1$  is depicted in Fig. 4. The velocity is normalized by the centerline velocity ( $U_{\max}$ ) corresponding to the classical laminar flow in the smooth microchannel. The non-dimensional groove width is adopted as  $w/D_h = 0.033$ , and the groove height is kept fixed for all the cases at  $H/D_h = 0.167$ . Also, the velocity profile of plain channel,  $P_{ch}$  (smooth wall) of  $D_h = 6 \mu\text{m}$  is shown along with the superhydrophobic micro/nano channel to differentiate the characteristic of velocity profile in the superhydrophobic micro/nano channel. One case of plain channel,  $D_h = 6 \mu\text{m}$  is shown here, as no variation is observed in the non-dimensional velocity profile for different values of  $D_h$ . It is observed that the velocity distribution is of parabolic shape for all the considered cases. As the shear stress is less at the mid-section of the channel, the maximum non-dimensional velocity is found at the middle of the channel for all the considered cases. When the superhydrophobic micro/nano groove is introduced, the velocity near the wall (at  $y/D = 0$  and  $y/D = 1$ ) is more than that of the  $P_{ch}$ , which signifies less wall shear stress developed in the superhydrophobic micro/nano channel due to the existence of gas layer. The velocity at near-wall region reduces with increasing  $D_h$ . When the channel is converted from micro- to nano-scale, the wall effect is less prominent on the flow and the wall shear stress decreases. The distance between the vertical parallel walls decreases with decreasing  $D_h$ , and the superhydrophobic surface area-to-fluid volume ratio increases. As a result, minor viscous effect is experienced by the flowing fluid when the channel hydraulic diameter is reduced.

In addition, a negative velocity zone or a recirculation zone of fluid inside the groove is observed for all the cases of considered  $D_h$ . For better visualization, an inset view of recirculation zone is shown in Fig. 4a and also an enlarged view of square dotted zone in red color shown in Fig. 4a for  $w/D_h = 0.033$  is depicted separately in Fig. 4b. This negative velocity zone confirms that the fluid flow in the groove is in the opposite direction of the main flow. The counteracting velocity or the vortex is formed due to flow continuity needs to be satisfied within the fluid that is trapped inside the triangular grooves. A similar observation is also found in earlier studies (Dey et al. 2018; Schäffel et al. 2016). The depth of the recirculation zone of trapped air decreases with increasing  $D_h$ . This decrease in depth of negative velocity zone is a consequence of

wall confinement effect on the same mass of fluid that flows within the channel with different values of  $D_h$ . In a higher  $D_h$  channel, the core flow zone is more and a lesser kinetic energy is transferred to the trapped gas and thus a smaller recirculation zone is observed to satisfy the continuity. Moreover, it is found that the velocity is not zero at the location where the plain walls exist, i.e., at  $y/D = 0$ . This characteristic reveals the existence of slip boundary condition at the solid–liquid interface for all the considered superhydrophobic micro/nano channel cases. The same phenomenon is also observed for the higher value of groove widths,  $w/D_h = 0.067$  and  $0.133$ . However, the recirculation zone and slip characteristics are more prominent in the higher groove widths, which are discussed later for all the considered configurations.

### 4.2 Effect of groove width on velocity distribution

The non-dimensional groove width is varied as  $w/D_h = 0$  (plain channel),  $0.033$ ,  $0.067$  and  $0.133$  and its effect on the velocity profile at  $Re = 1$  for two different values of  $D_h = 600 \text{ nm}$  and  $600 \mu\text{m}$  in the vicinity of the micro/nano grooves is shown in Fig. 5. As discussed earlier, the velocity profile is of parabolic shape for all the non-dimensional micro/nano groove configurations and for both the  $D_h$  values. After introducing the micro/nano grooves at the top and bottom walls of the plain micro/nano channel, the velocity near the wall region (at  $y/D = 0$  and  $y/D = 1$ ) increases than the plain micro/nano channel ( $w/D_h = 0$ ). The increment in velocity in these superhydrophobic micro/nano channels is due to the slip produced by trapped gas layer on the flowing liquid. It is observed that this near-wall velocity increases with increasing non-dimensional groove width for both the cases of  $D_h = 600 \text{ nm}$  and  $600 \mu\text{m}$ . When the micro/nano groove width is increased, the gas–liquid contact area increases and consequently, less wall shear stress is developed. As a result, flowing liquid experiences less frictional resistance and attains a larger velocity.

Moreover, within the superhydrophobic grooves, recirculation zone of trapped gas is also observed for all the considered cases as discussed earlier. For better visualization of recirculation zone for  $D_h = 600 \mu\text{m}$ , an inset view of recirculation zoned is shown in Fig. 5b. It is observed for both the micro and nano channels that the width and depth of the recirculation zone increase with increasing groove width. A large amount of air is trapped inside the wider grooves resulting in the decrease in wall shear stress and thus a larger recirculation zone is observed to satisfy the continuity. At the vicinity of the wall, the fluid velocity is non-zero for every width case, which signifies the slippage of liquid flow over the trapped gas layer inside the triangular grooves. Whereas, a zero velocity is

**Fig. 4 a** Non-dimensional velocity distribution for different values of  $D_h$  and **b** an enlarged view of velocity profile at near wall region

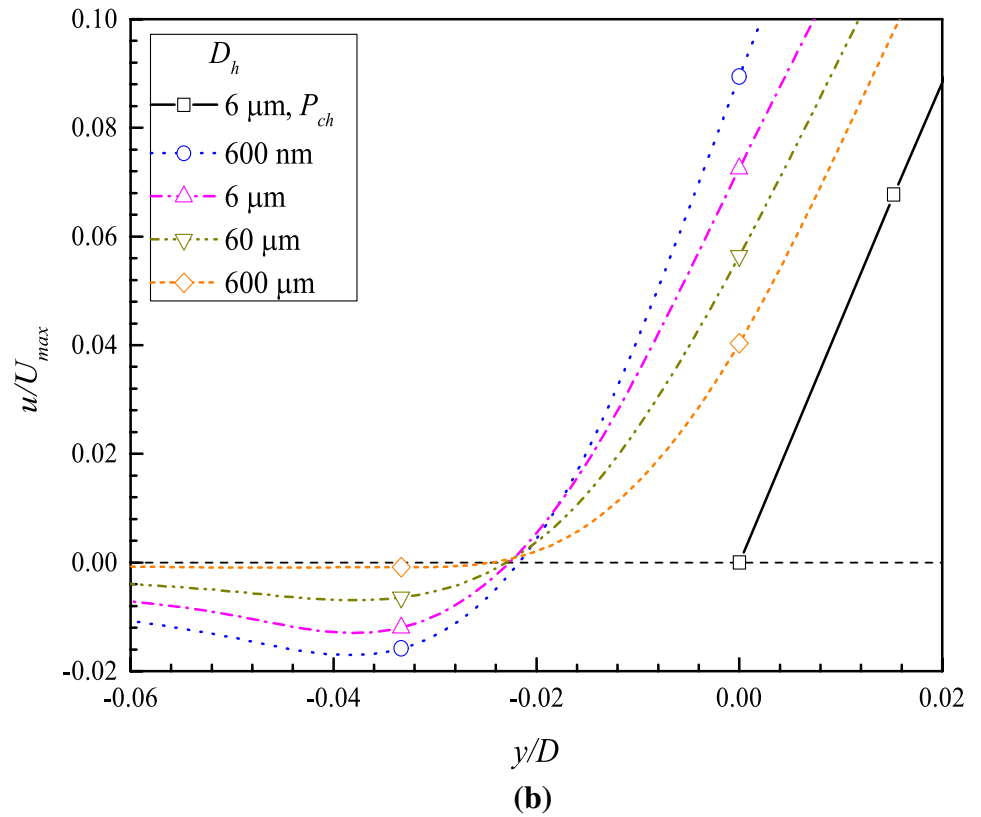
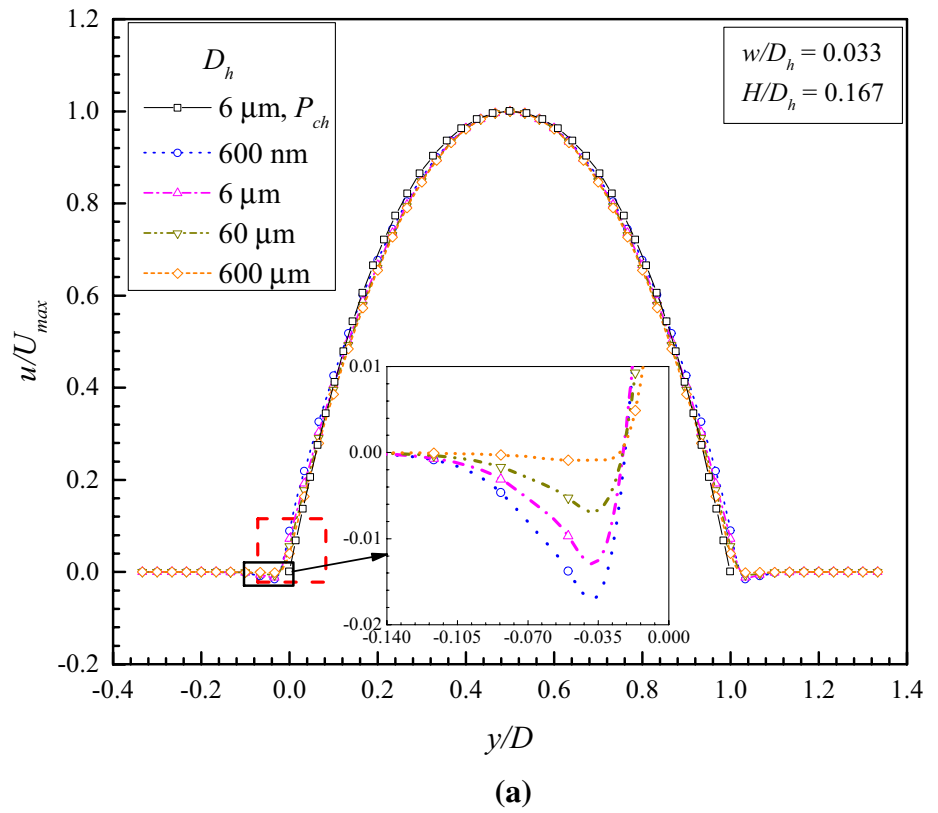
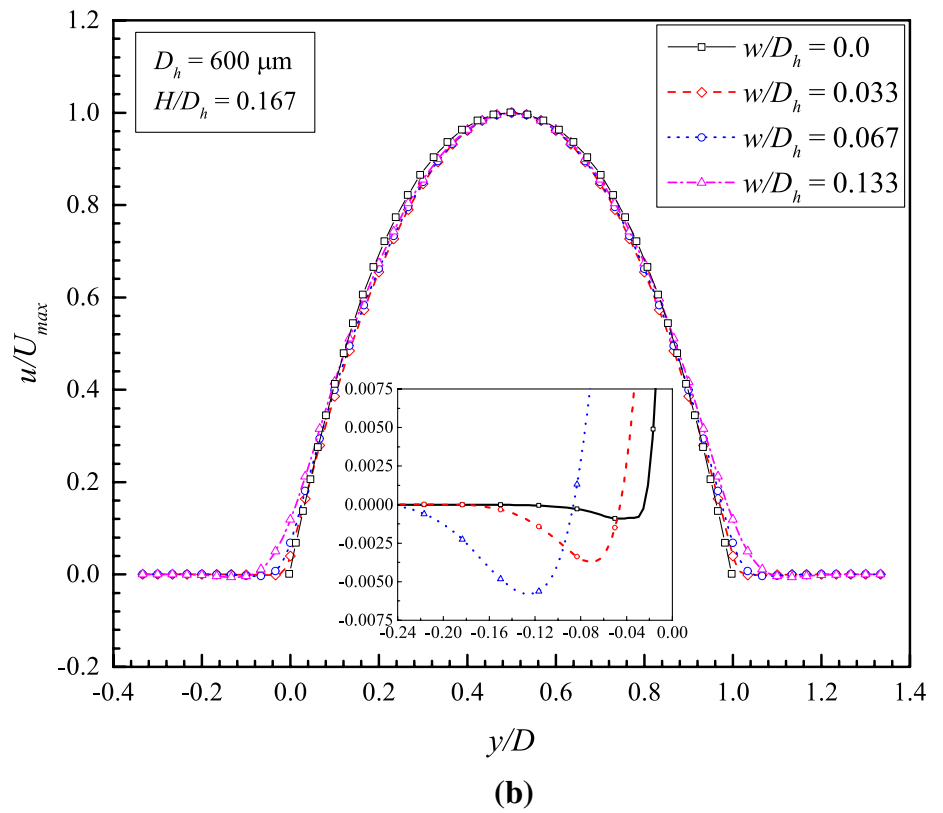
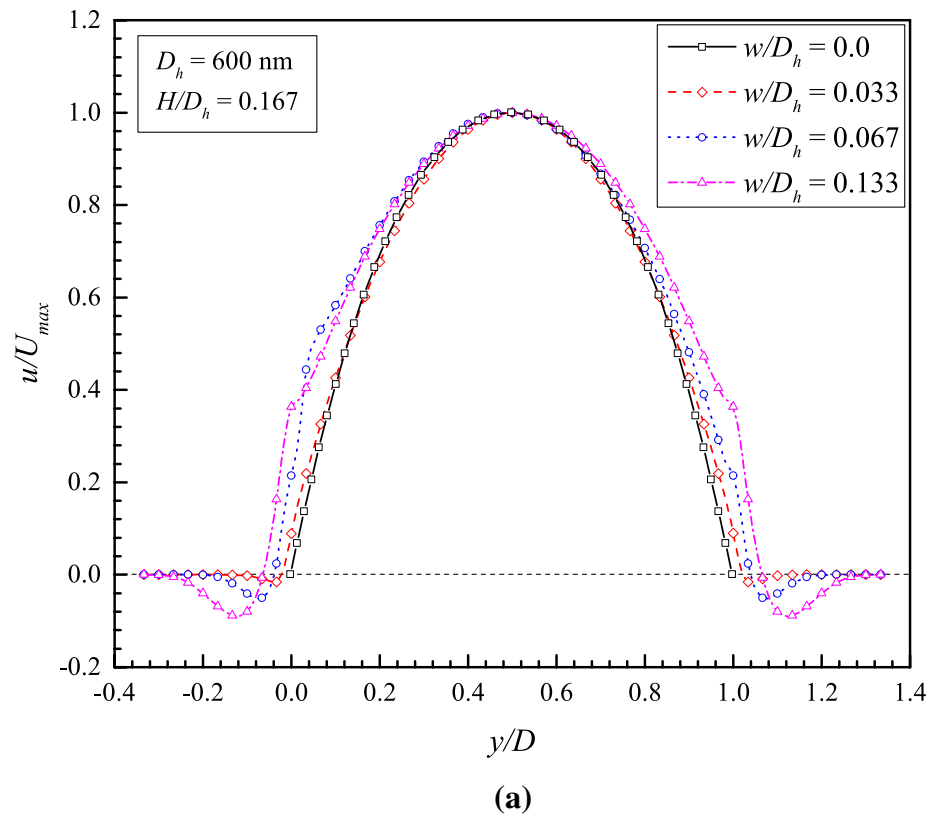




**Fig. 5** Effect of groove width on velocity profile for **a**  $D_h = 600$  nm (nanochannel) and **b**  $D_h = 600$   $\mu\text{m}$  (microchannel)



found in the plain channel for both the hydraulic diameter conditions.

### 4.3 Effect of channel confinement on slip properties

The effect of superhydrophobic triangular micro/nano grooves on the slippage of fluid flow over the trapped gas layer is characterized by the slip properties. The variation of normalized slip length ( $l_s/(D_h/2)$ ) and normalized slip velocity ( $u_s/U_{\max}$ ) for different groove widths and channel hydraulic diameters is shown in Fig. 6a, b, respectively. The slip length is normalized by the hydraulic diameter,  $D_h$  and the slip velocity is normalized by centerline velocity ( $U_{\max}$ ) in the channel. The slip length and slip velocity in a superhydrophobic surface can be related by Navier slip model and is expressed as,

$$u_s = l_s \frac{\partial u}{\partial y}, \text{ at } y = 0. \quad (24)$$

The constant of proportionality,  $l_s$  is called slip-length and is obtained by extrapolating the velocity profile normal to the slip surface.

It is observed from Fig. 6a that the normalized slip length increases with increasing channel hydraulic diameter. Also, the normalized slip length increases with the increment of groove width. However, the change in slip length with increasing  $D_h$  is not significant as compared to the change in slip length with increasing  $w/D_h$ . As discussed earlier, the velocity at the near-wall region is zero for the plain channel, thus the slip length is zero for all the configurations of plain channel. The increment in slip length is not noticeable for the lower-width superhydrophobic grooves compared to the higher micro/nano groove widths. The normalized slip length increases with increasing groove width for a certain channel hydraulic diameter, since the gas–liquid contact area increases with the increase in groove width. Accordingly, the solid–liquid contact area is decreased, resulting in the reduction of viscous drag.

The discrepancy of normalized slip velocity,  $u_s/U_{\max}$  for different groove widths,  $w/D_h = 0$  (plain channel), 0.033, 0.067 and 0.133 and for different channel hydraulic diameters,  $D_h = 600$  nm, 6  $\mu\text{m}$ , 60  $\mu\text{m}$  and 600  $\mu\text{m}$  at  $\text{Re} = 1$  is shown in Fig. 6b. A significant influence of hydraulic diameter and groove width can be observed from the figure. The normalized slip velocity,  $u_s/U_{\max}$  decreases with increasing  $D_h$ ; however,  $u_s/U_{\max}$  increases with the increase in  $w/D_h$ . The change in  $u_s/U_{\max}$  is significant when the channel hydraulic diameter tends to nano-scale compared to the channel with higher  $D_h$  values ( $\geq 60$   $\mu\text{m}$ ). For a given groove width, when the hydraulic diameter is decreased, the core flow zone decreases and the flowing fluid attains a higher velocity. Thus, the slip velocity at the gas–liquid interface

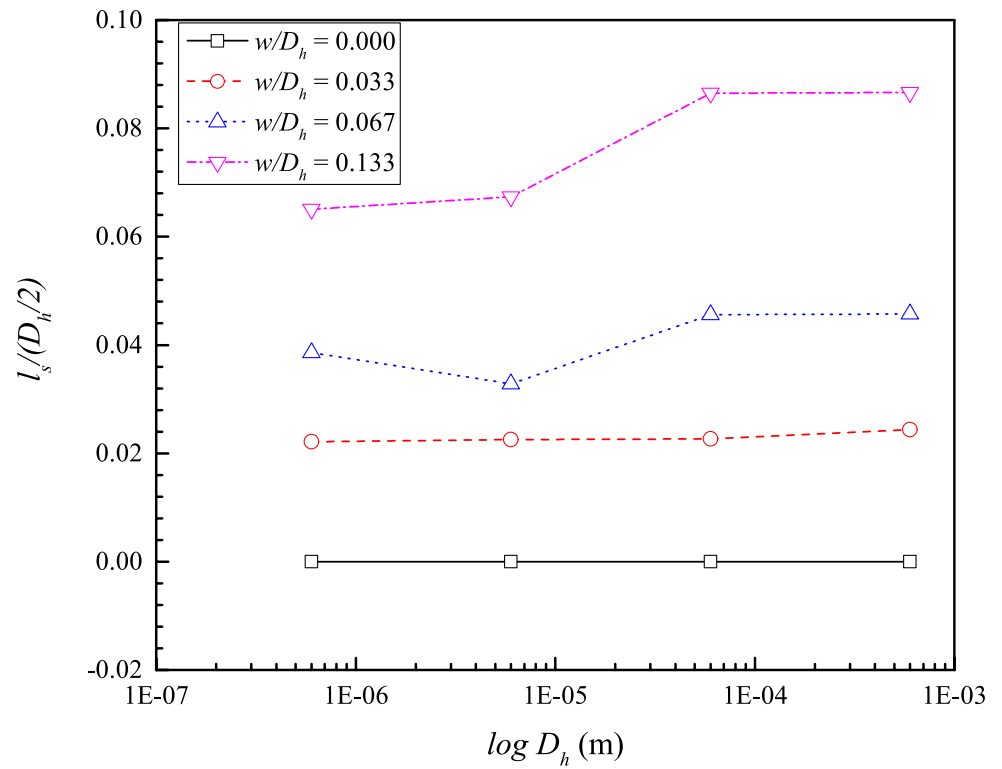
increases. As discussed earlier, when the superhydrophobic grooves width increases, the gas–liquid contact area increases and accordingly, higher slip of the flowing liquid is generated by the trapped gas inside the grooves.

### 4.4 Effect of channel confinement on meniscus shape and position

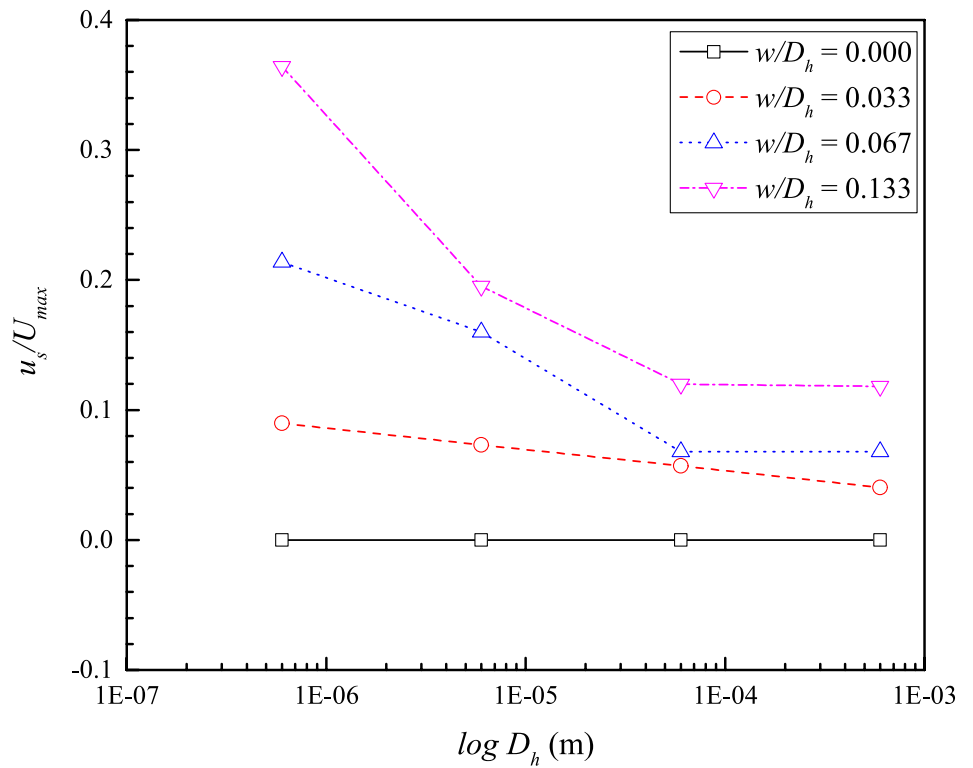
It was observed that the gas–liquid interface is significantly influenced by the flow conditions and the microgroove geometry (Dey et al. 2018). Thus, in this study, the effect of channel confinement and micro/nano groove width for a constant flow condition is investigated and the corresponding variation of interface position inside the groove ( $P_d$ ) and apparent contact angle ( $\theta_{\text{app}}$ ) are shown in Fig. 7a, b, respectively. The position of the interface inside the micro/nano grooves is calculated from the distance between the interface location at middle of the triangular groove and the top surface of that groove. The schematic representation of the interface position ( $P_d$ ) and the apparent contact angle ( $\theta_{\text{app}}$ ) are shown in the inset view of Fig. 7a, b. The negative value of  $P_d$  denotes the interface position inside the grooves, whereas the positive value indicates the interface position above the grooves. The location of the interface inside the grooves increases with increasing hydraulic diameter for every considered groove width. In the larger  $D_h$  channels, the interface penetrates more into the grooves, resulting in a higher solid–liquid contact area. However, when the microchannel is converted into a nanochannel ( $D_h = 600$  nm), the interface is located near the top of the groove and this characteristic of interface reveals more gas–liquid contact area in a nanochannel, resulting in the reduction of frictional resistance at the solid–liquid contact area. It is also observed that the interface position inside the triangular grooves increases with increasing groove width. In the wider micro/nano groove ( $w/D_h = 0.133$ ), the position of the interface inside the groove is more than the narrower groove for a certain value of  $D_h$ . The interaction between the trapped gas and flowing liquid is higher in wider grooves resulting in more suppression of gas phase by the liquid phase inside the grooves.

The gas–liquid interface may be of different shapes, such as flat, concave or convex depending on several conditions (Dey et al. 2018). The effect of channel hydraulic diameter from micro- to nano-scale on the interface shape is also investigated for different groove widths and is shown in Fig. 7b. The interface shape is represented by apparent contact angle ( $\theta_{\text{app}}$ ) which is the angle between the tangent at the interface and the vertical line drawn at the triple point and the schematic representation of  $\theta_{\text{app}}$  is depicted in the inset view of Fig. 7b. The value of apparent contact angle,  $\theta_{\text{app}} = 90^\circ$  represents flat interface shape, whereas,  $\theta_{\text{app}} < 90^\circ$  and  $\theta_{\text{app}} > 90^\circ$  signify the interface shape as convex and concave, respectively. It is observed that the interface shape is greatly influenced by  $D_h$ . The

**Fig. 6** Effect of channel confinement on **a** normalized slip length and **b** normalized slip velocity

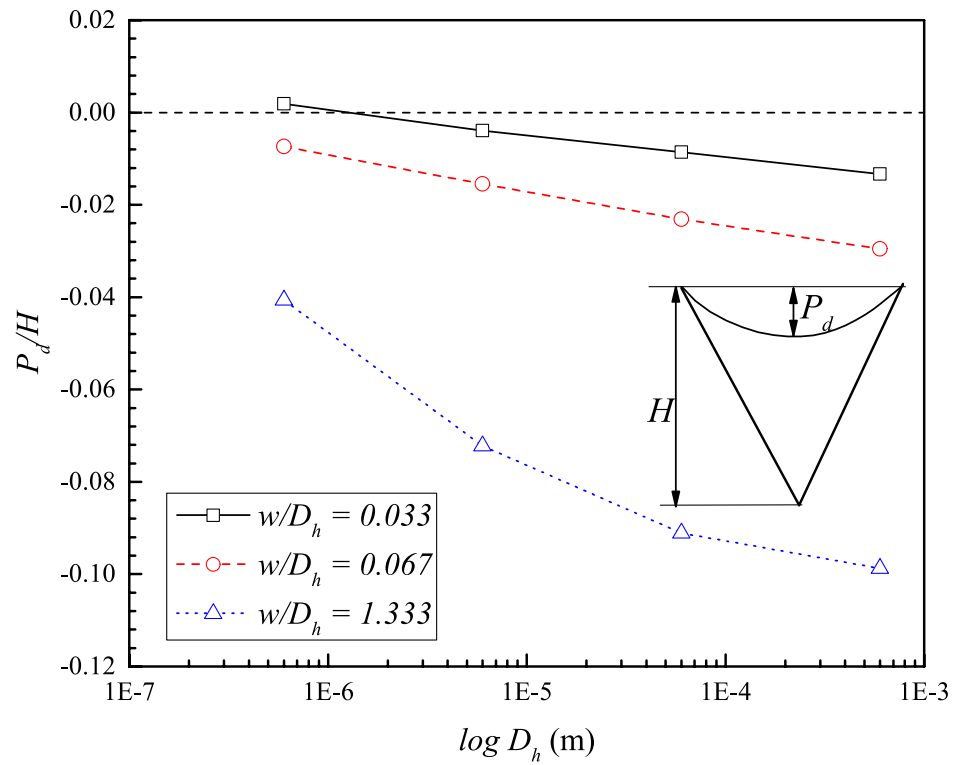


**(a)**

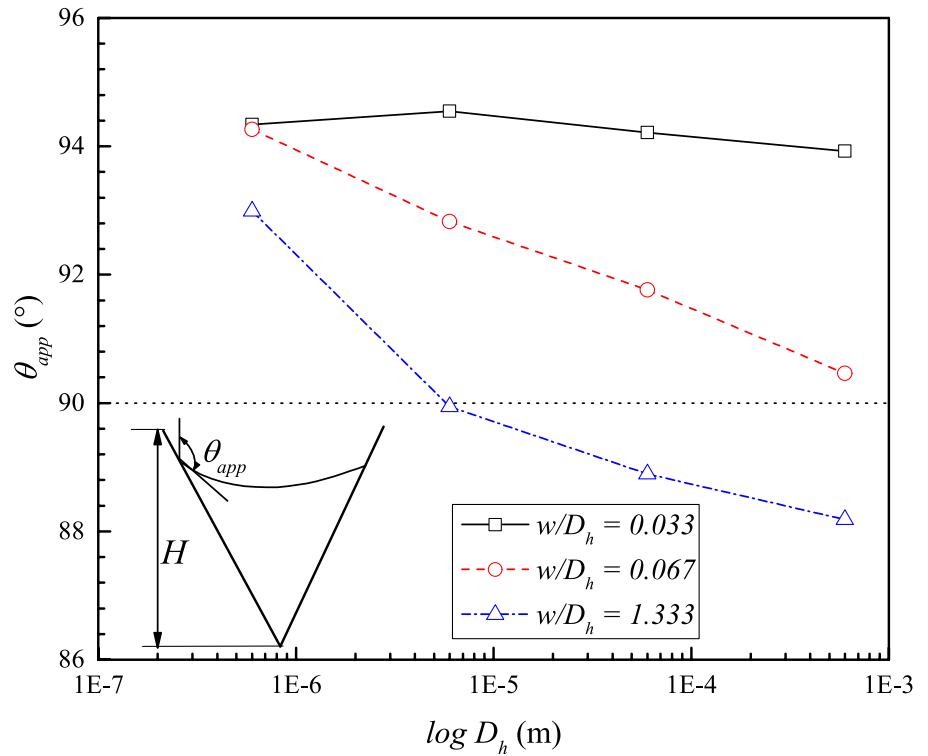


**(b)**

**Fig. 7** Effect of channel confinement on **a** interface position and **b** interface shape



**(a)**



**(b)**

apparent contact angle increases with decreasing  $D_h$ . When the channel is converted to nano- from micro-scale, the interface shape becomes concave from convex followed by flat one. The micro/nano groove width has significant effect on  $\theta_{app}$  and it is found that the  $\theta_{app}$  decreases with increasing groove width,  $w/D_h$ . The variation of  $\theta_{app}$  for narrower grooves is less prominent than the wider grooves. The interface shape is found as concave at  $w/D_h = 0.033$  and 0.067 for every considered values of  $D_h$ . However, the shape is observed as concave, flat and convex at  $w/D_h = 0.133$  when the channel is changed to micro- from the nano-scale.

### 4.5 Effect of channel confinement on pressure drop reduction

The primary objective of using superhydrophobic surface in a channel is to reduce the frictional drag or the pumping power by developing slip by the entrapped gas layer on the flowing liquid. Thus, the effect of channel confinement on the non-dimensional pressure drop reduction is investigated for different groove widths and is shown in Fig. 8. The percentage reduction of non-dimensional pressure drop ( $\pi$ ) is calculated as,

$$\pi = \frac{\Delta P_{P_{ch}} - \Delta P_{SH_{ch}}}{\Delta P_{P_{ch}}} \times 100\%, \tag{25}$$

where,  $P_{ch}$  denotes the plain channel without superhydrophobic grooves and  $SH_{ch}$  is the superhydrophobic channels

with triangular grooves. It can be observed that the  $\pi$  reduces with increasing hydraulic diameter. When the scale of channel hydraulic diameter changes from micro to nano, the percentage reduction of pressure drop is found more than 52% for the groove width,  $w/D_h = 0.133$ . This is because the superhydrophobic surface area-to-fluid volume ratio is increased when the channel hydraulic diameter is changed to nano-scale. As a result, the effect of the superhydrophobic surface is prominent, thereby increasing the drag reduction effect in nano-scale channel. A similar observation was found experimentally (Ou et al. 2004) and numerically (Li et al. 2016) when the microchannel height is reduced; however, the height of the channel was still in micro-scale. Also, the pressure drop is significantly reduced when the groove width increases. As discussed earlier, with increasing groove width for a certain channel hydraulic diameter, the gas-liquid contact area increases with the increase in groove width. Accordingly, the solid-liquid contact area is decreased resulting in the reduction of viscous drag and thus the pressure drop reduction increases with increasing groove width.

In addition, a comparison between the percentage reduction of pressure drop, obtained in the present study and reported by the published experimental and numerical analyses, is summarized in Table 2. It can be observed that a minimum of 10% in pressure drop reduction was achieved for high Reynolds number application using superhydrophobic coating (Gogte et al. 2005). However, a maximum of 76% was obtained numerically by utilizing square microposts at  $Re = 1$  (Cheng et al. 2009). It can be noted that the

**Fig. 8** Effect of channel confinement on the percentage pressure drop reduction

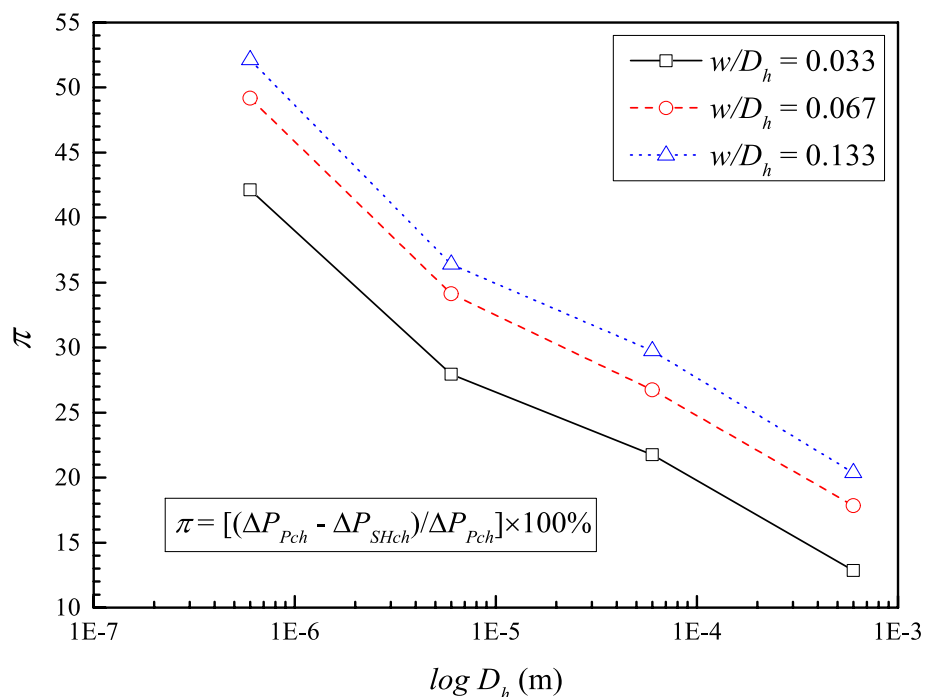


**Table 2** A comparative study of pressure drop reduction with published literature

	Experimental/ numerical	SPHs type	$D_h$ ( $\mu\text{m}$ ) and Re	$\Pi$ (%)
Ou et al. (2004)	Both	Patterned rectangular groove	$144.76 \leq D_h \leq 483.8$ $\text{Re} < 1000$	40
Gogte et al. (2005)	Experiment	Superhydrophobic coating	$1500 \leq \text{Re} \leq 11,000$ (Based on length) length, $L = 4.3$ cm	10
Samaha et al. (2011)	Numerical	Particles or microposts	$D_h$ (not available) $11.85 \leq \text{Re} \leq 1778$	30
Cheng et al. (2015)	Numerical	Square micropost	$\text{Re} = 1$	76
Das and Bhaumik (2018)	Experiment	Lotus leaf replica	Cylindrical channel with diameter $125 \mu\text{m}$	35
Motamedi et al. (2019)	Experiment	Straight ribs-and-grooves	$D_h = 266.66$ $20 \leq \text{Re} \leq 60$	19
Present study	Numerical	Triangular microgroove	$0.6 \leq D_h \leq 600$ $\text{Re} = 1$	52

air-interface was assumed as flat by the authors and a shear-free boundary condition was applied at the presumed interface, which was found less precise than the no-slip boundary condition when compared with the experimental results (Kim and Hidrovo 2012; Song et al. 2018). In the present study, a no-slip boundary condition at the microgroove walls without predefining the interface is applied, which is found more agreeable with the experimental results than the results obtained by employing shear-free boundary condition and is also found to be consistent with the other studies. Accordingly, a maximum pressure drop reduction of 52% is achieved in the present analysis.

## 5 Conclusions

We present a comprehensive numerical analysis of the effect of channel confinement on the dynamical evolution of a liquid–gas interface, the resulting slip characteristics, and the corresponding possibilities in drag reduction over superhydrophobic triangular grooves. It is found that the flowing fluid is significantly affected not only by the channel confinement, but also considerably affected by the groove width. However, the superhydrophobic surface area-to-fluid volume ratio has more pronounced effect on the velocity of the flowing fluid. For a certain groove width, the fluid near the wall attains a larger velocity in nanochannel than a microchannel. This is primarily due to extreme confined nature of the physical system. Accordingly, a large amount of slip on the fluid by the gas layer can be obtained by reducing the scale of the domain from micro to nano, premised on the same grooved structure. The interface shape may turn out to be flat, concave and convex, depending on the combined consequences of the channel dimensions and the groove width. In addition, the percentage reduction of pressure drop can be increased by a large amount as we transit

from micro-scale to nano-scale paradigm where the surface area-to-fluid volume ratio is high and also the groove width has prominent influence on pressure drop reduction. These findings may be of significant implications towards designing a superhydrophobic micro and nanochannel for a wide variety of applications ranging from engineering to biology.

**Acknowledgements** SC acknowledges Department of Science and Technology, Government of India, for Sir J. C. Bose National Fellowship.

## References

- Afkhami S, Bussmann M (2008) Height functions for applying contact angles to 2D VOF simulations. *Int J Numer Methods Fluids* 57:453–472
- Brackbill JU, Kothe DB, Zemach C (1992) A continuum method for modeling surface tension. *J Comput Phys* 100:335–354
- Chakraborty S (2007) Towards a generalized representation of surface effects on pressure-driven liquid flow in microchannels. *Appl Phys Lett* 90:034108
- Chakraborty D, Dingari NN, Chakraborty S (2012) Combined effects of surface roughness and wetting characteristics on the moving contact line in microchannel flows. *Langmuir* 28:16701–16710
- Chakraborty S, Chatterjee D, Bakli C (2013) Nonlinear amplification in electrokinetic pumping in nanochannels in the presence of hydrophobic interactions. *Phys Rev Lett* 110:184503
- Chen H, Li L, Zhang T, Qiao Z, Tang J, Zhou J (2018) Protein translocation through a MoS<sub>2</sub> nanopore: a molecular dynamics study. *J Phys Chem C* 122:2070–2080
- Cheng Y, Teo C, Khoo B (2009) Microchannel flows with superhydrophobic surfaces: effects of Reynolds number and pattern width to channel height ratio. *Phys Fluids* 21:122004
- Cheng Y, Xu J, Sui Y (2015) Numerical study on drag reduction and heat transfer enhancement in microchannels with superhydrophobic surfaces for electronic cooling. *Appl Therm Eng* 88:71–81
- Choi C-H, Kim C-J (2006) Large slip of aqueous liquid flow over a nanoengineered superhydrophobic surface. *Phys Rev Lett* 96:066001

- Cummins SJ, Francois MM, Kothe DB (2005) Estimating curvature from volume fractions. *Comput Struct* 83:425–434
- Das A, Bhaumik SK (2018) Fabrication of cylindrical superhydrophobic microchannels by replicating lotus leaf structures on internal walls. *J Micromech Microeng* 28:045011
- Davies J, Maynes D, Webb B, Woolford B (2006) Laminar flow in a microchannel with superhydrophobic walls exhibiting transverse ribs. *Phys Fluids* 18:087110
- Dey P, Saha SK, Chakraborty S (2018) Microgroove geometry dictates slippery hydrodynamics on superhydrophobic substrates. *Phys Fluids* 30:122007
- Francois MM, Cummins SJ, Dendy ED, Kothe DB, Sicilian JM, Williams MW (2006) A balanced-force algorithm for continuous and sharp interfacial surface tension models within a volume tracking framework. *J Comput Phys* 213:141–173
- Fürstner R, Barthlott W, Neinhuis C, Walzel P (2005) Wetting and self-cleaning properties of artificial superhydrophobic surfaces. *Langmuir* 21:956–961
- Gaddam A, Agrawal A, Joshi SS, Thompson M (2015) Utilization of cavity vortex to delay the wetting transition in one-dimensional structured microchannels. *Langmuir* 31:13373–13384
- Genzer J, Efimenko K (2006) Recent developments in superhydrophobic surfaces and their relevance to marine fouling: a review. *Biofouling* 22:339–360
- Gogte S, Vorobieff P, Truesdell R, Mammoli A, van Swol F, Shah P, Brinker CJ (2005) Effective slip on textured superhydrophobic surfaces. *Phys Fluids* 17:051701
- Greenshields CJ (2015) OpenFOAM: The Open Source CFD Toolbox, User Guide OpenFOAM Foundation Ltd
- Hirt CW, Nichols BD (1981) Volume of fluid (VOF) method for the dynamics of free boundaries. *J Comput Phys* 39:201–225
- Holt JK et al (2006) Fast mass transport through sub-2-nanometer carbon nanotubes. *Science* 312:1034–1037
- Holzmann T (2016) Mathematics, numerics, derivations and OpenFOAM®. Loeben. Holzmann CFD, Germany
- Jung YC, Bhushan B (2009) Wetting behavior of water and oil droplets in three-phase interfaces for hydrophobicity/philicity and oleophobicity/philicity. *Langmuir* 25:14165–14173
- Kim TJ, Hidrovo C (2012) Pressure and partial wetting effects on superhydrophobic friction reduction in microchannel flow. *Phys Fluids* 24:112003
- Lauga E, Stone HA (2003) Effective slip in pressure-driven Stokes flow. *J Fluid Mech* 489:55–77
- Lee C, Choi C-H (2008) Structured surfaces for a giant liquid slip. *Phys Rev Lett* 101:064501
- Li C, Zhang S, Xue Q, Ye X (2016) Simulation of drag reduction in superhydrophobic microchannels based on parabolic gas–liquid interfaces. *Phys Fluids* 28:102004
- Liu T, Kim C-J (2014) Turning a surface superrepellent even to completely wetting liquids. *Science* 346(6213):1096–1100
- Malik M, Fan ESC, Bussmann M (2007) Adaptive VOF with curvature-based refinement. *Int J Numer Meth Fluids* 55:693–712
- Maynes D, Jeffs K, Woolford B, Webb B (2007) Laminar flow in a microchannel with hydrophobic surface patterned microribs oriented parallel to the flow direction. *Phys Fluids* 19:093603
- McHale G, Shirtcliffe N, Evans C, Newton M (2009) Terminal velocity and drag reduction measurements on superhydrophobic spheres. *Appl Phys Lett* 94:064104
- Motamedi M, Chung C-Y, Rafeie M, Hjerrild N, Jiang F, Qu H, Taylor A, Taylor RA (2019) Experimental testing of hydrophobic microchannels, with and without nanofluids, for solar PV/T collectors. *Energies* 12:3036
- Ng C-O, Wang C (2009) Stokes shear flow over a grating: implications for superhydrophobic slip. *Phys Fluids* 21:087105
- Nosonovsky M, Bhushan B (2009) Superhydrophobic surfaces and emerging applications: non-adhesion, energy, green engineering. *Curr Opin Colloid Interf Sci* 14:270–280
- Ou J, Rothstein JP (2005) Direct velocity measurements of the flow past drag-reducing ultrahydrophobic surfaces. *Phys Fluids* 17:103606
- Ou J, Perot B, Rothstein JP (2004) Laminar drag reduction in microchannels using ultrahydrophobic surfaces. *Phys Fluids* 16:4635–4643
- Rusche H (2003) Computational fluid dynamics of dispersed two-phase flows at high phase fractions. Imperial College London (University of London)
- Samaha MA, Vahedi Tafreshi H, Gad-el-Hak M (2011) Modeling drag reduction and meniscus stability of superhydrophobic surfaces comprised of random roughness. *Phys Fluids* 23:012001
- Schäffel D, Koynov K, Vollmer D, Butt H-J, Schönecker C (2016) Local flow field and slip length of superhydrophobic surfaces. *Phys Rev Lett* 116:134501
- Song D, Song B, Hu H, Du X, Du P, Choi C-H, Rothstein JP (2018) Effect of a surface tension gradient on the slip flow along a superhydrophobic air–water interface. *Phys Rev Fluids* 3:033303
- Sussman M (2003) A second order coupled level set and volume-of-fluid method for computing growth and collapse of vapor bubbles. *J Comput Phys* 187:110–136
- Teo CJ, Khoo BC (2010) Flow past superhydrophobic surfaces containing longitudinal grooves: effects of interface curvature. *Microfluid Nanofluid* 9:499–511
- Teo C, Khoo B (2014) Effects of interface curvature on Poiseuille flow through microchannels and microtubes containing superhydrophobic surfaces with transverse grooves and ribs. *Microfluid Nanofluid* 17:891–905
- Tsai P, Peters AM, Pirat C, Wessling M, Lammertink RG, Lohse D (2009) Quantifying effective slip length over micropatterned hydrophobic surfaces. *Phys Fluids* 21:112002
- Van Leer B (1977) Towards the ultimate conservative difference scheme III. Upstream-centered finite-difference schemes for ideal compressible flow. *J Comput Phys* 23:263–275
- Van Leer B (1979) Towards the ultimate conservative difference scheme. V. A second-order sequel to Godunov’s method. *J Comput Phys* 32:101–136
- Weller H (1993) The development of a new flame area combustion model using conditional averaging Thermo-fluids section report TF 9307
- Weller HG (2008) A new approach to VOF-based interface capturing methods for incompressible and compressible flow OpenCFD Ltd, Report TR/HGW 4
- Woolford B, Jeffs K, Maynes D, Webb B (2005) Laminar fully-developed flow in a microchannel with patterned ultrahydrophobic walls. In: ASME 2005 Summer Heat Transfer Conference collocated with the ASME 2005 Pacific Rim Technical Conference and Exhibition on Integration and Packaging of MEMS, NEMS, and Electronic Systems, 2005. American Society of Mechanical Engineers, pp 481–488
- Zhao S, Xue J, Kang W (2013) Ion selection of charge-modified large nanopores in a graphene sheet. *J Chem Phys* 139:114702

**Publisher’s Note** Springer Nature remains neutral with regard to jurisdictional claims in published maps and institutional affiliations.